Thermal decomposition of dolomite under CO_2: Insights from TGA and in-situ XRD analysis

Jose Manuel Valverde[a*], Antonio Perejon[b], Santiago Medina[c], Luis A. Perez-Maqueda[d]

[a] Faculty of Physics. University of Seville. Avenida Reina Mercedes s/n, 41012 Sevilla, Spain

[b] Faculty of Chemistry. University of Seville. C/ Profesor Garcia Gonzalez s/n, 41012 Sevilla, Spain

[c] X-Ray Laboratory (CITIUS), University of Seville, Avenida Reina Mercedes, 4B. 41012 Sevilla, Spain

[d] Instituto de Ciencia de Materiales de Sevilla (C.S.I.C.-Univ. Seville), Americo Vespucio 49, 41092 Sevilla, Spain

* Corresponding Author: Fax: +34 95423 9434; Tel: +34 95455 0960; E-mail: jmillan@us.es

Abstract

Thermal decomposition of dolomite in the presence of CO_2 in the calcination environment is investigated by means of in-situ X-ray diffraction (XRD) and thermogravimetric analysis (TGA). In-situ XRD results suggest that dolomite decomposes directly at a temperature around 700°C into MgO and CaO. Immediate carbonation of the nascent CaO crystals leads to the formation of calcite as intermediate product of decomposition. Subsequently, decarbonation of this poorly crystalline calcite occurs when the reaction is thermodynamically favorable and sufficiently fast at a temperature depending on the CO_2 partial pressure in the calcination atmosphere. Decarbonation of this dolomitic calcite occurs at a lower temperature than limestone decarbonation due to the relatively lower crystallinity of the former. Full decomposition of dolomite leads also to a relatively low crystalline CaO, which exhibits a relatively high reactivity as compared to limestone derived CaO. At CO_2 capture conditions in the Calcium-Looping (CaL) process, MgO grains remain inert yet favor the carbonation reactivity of dolomitic CaO specially in the solid-state diffusion controlled phase. The fundamental mechanism that drives the crystallographic transformation of dolomite in the presence of CO_2 is thus responsible for its fast calcination kinetics and the high carbonation reactivity of dolomitic CaO, which makes natural dolomite a potentially advantageous alternative to limestone for CO_2 capture in the CaL technology as well as SO_2 in-situ removal in oxy-combustion fluidized bed reactors.

I. INTRODUCTION

Recent studies on the conservation of cultural heritage have revealed that the use of dolomitic lime (MgO·CaO) derived from calcination of dolomite ($CaMg(CO_3)_2$) as binder in mortars was a generalized practice in ancient masonry [1]. Dolomitic lime mortars had higher strength and resistance to deterioration than lime (CaO) mortars derived from limestone ($CaCO_3$) calcination [1–3] if their preparation followed certain specific rules. Archeological records show that dolomite thermal decomposition in ancient ovens was carried out under high CO_2 concentration at relatively low temperatures, which highlights the extraordinary relevance of calcination conditions on the structural and physicochemical characteristics of the calcium and magnesium oxides produced during thermal decomposition. Nowadays, the thermal decomposition of dolomite under CO_2 remains at the root of a number of industrial processes aimed at using Ca and Mg oxides and carbonates as raw materials for the production of portland cement and Mg-based products, respectively [4].

Natural limestone and dolomite have been used commercially in the energy sector industry since the 1970s for SO_2 capture in fluidized bed coal combustors [5, 6]. CaO resulting from in-situ thermal decomposition undergoes sulphation ($CaO+SO_2+\frac{1}{2}O_2 \rightarrow CaSO_4$) at temperatures between 800 and 900°C at a rate that depends on the partial pressure of CO_2 in the calcination environment. During fluidized bed atmospheric combustion (with typically 20% excess air), the partial pressure of the generated CO_2 is about 0.15 atm. On the other hand, in the close to commercial oxy-combustion technology for CO_2 capture, the concentration of CO_2 in the flue gas is enriched up to ∼95% by burning the fuel with a mixture of nearly pure oxygen and a CO_2 rich recycled flue gas at combustor temperatures typically between 850°C and 950°C. Thermal decomposition of limestone under high CO_2

partial pressure ($P \simeq 1$ atm) occurs sufficiently fast only at temperatures above 930°C [7, 8]. Thus, SO_2 retention in the oxy-combustion reactor would occur by the less efficient direct sulphation reaction ($CaCO_3 + SO_2 + 1/2O_2 \rightarrow CaSO_4 + CO_2$) [9, 10]. Another promising CO_2 capture process, which has been identified as a cost-effective approach, is the recently emerged Ca-looping (CaL) technology based on the multicyclic calcination/carbonation of $CaCO_3$ using natural limestone as raw material [11–13]. In this post-combustion capture technology, the combustor effluent gas at atmospheric pressure with typically 15% vol concentration of CO_2 is used for fluidization of CaO particles in a gas-solid reactor (carbonator) wherein CO_2 is retained by carbonation of CaO at optimum temperatures around 650°C. The carbonated solids are driven into a second fluidized bed reactor (calciner) in which $CaCO_3$ is regenerated by calcination under CO_2 at high partial pressure. In order to obtain a stream of highly concentrated CO_2 from the calciner and to rise its temperature up to high enough values, fuel is burned in-situ in the calciner by oxy-combustion [14, 15]. Since natural limestone decomposition under CO_2 partial pressures close to $P = 1$ atm is extremely slow near to equilibrium conditions ($T \simeq 895$°C) [7, 8], the calciner temperature in practice has to be increased up to $T \simeq 930$°C in order to achieve a high calcination efficiency, which imposes an important energy penalty to the technology [12, 13, 16]. Furthermore, the decay of CaO carbonation reactivity with the number of cycles must be compensated by periodically feeding the calciner with a makeup flow of fresh limestone while a fraction of the circulating sorbent is purged.

Thermogravimetric analysis (TGA) indicates that the use of dolomite as CaO precursor in a calcination environment of high CO_2 partial pressure would allow reducing the calcination temperature as compared to limestone [17]. The use of dolomite would thus presumably improve the in-situ SO_2 capture performance in oxyfuel combustors as well as the calciner

efficiency in the CaL technology. Moreover, the decay of carbonation reactivity of dolomitic CaO with the number of calcination/carbonation cycles at CaL conditions is mitigated [17–21]. The main purpose of the present work is to understand the fundamental mechanisms that drives this behavior. To this end, the calcination reaction of natural dolomite, as affected by the CO_2 partial pressure in the calciner atmosphere, will be investigated by means of in-situ X-ray diffraction (XRD) analysis coupled with TGA at similar conditions.

II. MECHANISM OF DOLOMITE THERMAL DECOMPOSITION

TGA and differential thermal analysis (DTA) have long demonstrated that the CO_2 partial pressure in the calcination environment determines essentially the mechanism of dolomite thermal decomposition [4, 22–24]. At CO_2 partial pressures below $P \simeq 0.1$ atm decomposition of dolomite into CaO and MgO is observed to occur apparently via a single stage reaction:

$$CaMg(CO_3)_2 \rightarrow CaO + MgO + 2CO_2 \tag{1}$$

In-situ XRD analysis of calcination at low absolute pressures ($< 10^{-6}$ bar) and low temperatures (490 - 600°C) [25] as well as in-situ TEM observations by exposure of dolomite to an e-beam under vacuum [26, 27] have revealed that pure CaO and MgO crystals nucleate from a metastable FCC solid solution $Mg_{0.5}Ca_{0.5}O$, which stems as a direct result of dolomite breakdown by a topotactic process. Transient Mg-rich CaO ($Ca_\epsilon\ Mg_{1-\epsilon}O$) and Ca-rich MgO crystals ($Mg_\delta Ca_{1-\delta}O$, with $\epsilon \sim \delta \sim 0.1$) are identified as resulting from the equimolar solid solution [25, 27], which is thermodynamically unstable because of the mismatch of cation sizes (the equilibrium solid solution contains at most 8 mol% Ca in MgO and 22 mol% Mg

in CaO [26]). Pure CaO and MgO crystals form afterwards by diffusion of Ca^{2+} and Mg^{2+} ions across the phase boundary between the mixed oxide crystallites.

Decomposition under CO_2 at partial pressures higher than about 0.1 atm consists of a two-stage process. As temperature is increased, the first and simultaneously emerging products of dolomite decomposition are calcite ($CaCO_3$) and periclase (MgO) whereas $CaCO_3$ decomposition takes place subsequently at a higher temperature to form CaO:

$$CaMg(CO_3)_2 \rightarrow CaCO_3 + MgO + CO_2 \tag{2}$$

$$CaCO_3 \rightarrow CaO + CO_2 \tag{3}$$

Experimental TG and DTA results show that the so-called half-decomposition of dolomite (reaction 2) is not fundamentally affected by the CO_2 partial pressure P whereas decomposition of $CaCO_3$ (reaction 3) is shifted towards higher temperatures as the CO_2 partial pressure P is increased [23, 24] according to the thermodynamic equilibrium of the $CaCO_3$ calcination reversible reaction [8, 28]:

$$P(\text{atm}) \approx 4.083 \times 10^7 \exp(-20474/T_{eq}) \tag{4}$$

where T_{eq} is the temperature for the reaction to be at equilibrium 3.

The physicochemical mechanism that governs dolomite half-decomposition under the presence of CO_2 remains a controverted issue [2, 3, 22, 27, 29, 30]. Traditionally, it was believed that calcite and magnesite ($MgCO_3$) microdomains were initially developed by the counter current diffusion of Mg^{2+} and Ca^{2+} ions [29]:

$$CaMg(CO_3)_2 \rightarrow CaCO_3 + MgCO_3 \tag{5}$$

Half-decomposition would thus obey to the thermodynamical instability of $MgCO_3$ at relatively lower temperatures than $CaCO_3$ [18, 31]. However, the equilibrium temperature of magnesite decomposition under pure CO_2 at atmospheric pressure would be around 400°C [18]. In contrast, half-decomposition is generally observed at higher temperatures (around 700°C) [32] in non-isothermal tests usually carried out at low heating rates ($\sim$ 10°C/min), which could be nevertheless explained from the existence of a certain activation energy for ion diffusion [22, 29]. In fact, half-decomposition is observed at comparable temperatures with that at which magnesite itself decomposes ($T \sim 400$ °C) for dolomite samples previously subjected to prolonged and vigorous grinding that would arguably promote the migration of Mg^{2+} and Ca^{2+} ions [29, 33].

Other decomposition mechanisms proposed contemplate the formation of calcite/magnesite ($CaCO_3$(1-n)$MgCO_3$) [34] and calcite/MgO ((1-x)$CaCO_3$(1-y)MgO) intermediates near to equilibrium as suggested from ex-situ XRD analysis [3]. An alternative view is that MgO and CaO crystals are directly generated during the breakdown of the dolomite structure, which is immediately followed by the direct carbonation of the nascent CaO crystals at temperatures below the thermal decomposition of calcite (T_{eq} in Eq. 4) [4, 22–24]. Accordingly, a recent study based on ex-situ XRD/2D-XRD analysis and FESEM/TEM observations [27] suggests that dolomite decomposition in air follows a similar mechanistic path to that found under vacuum [27]. Yet, the occurrence of dolomite decomposition in air at higher temperatures (650-700°C) than in vacuum would enhance ion diffusion [27]. Thus, Mg-calcite crystals would be initially formed by carbonation of the nascent $Mg_\delta Ca_{1-\delta}O$ ($\delta \leq 0.1$) phase with CO_2 present in the air and/or released upon decomposition [27]. As the temperature is further increased, Mg^{2+} ions diffuse out of the Mg-calcite structure, after which calcite would decompose at $T > 750$°C to yield pure CaO and MgO as final products [27].

The present study is focused on analyzing the structural evolution of dolomite under atmospheric pressure as it suffers thermal decomposition in the presence of CO_2 at partial pressures ranging between 0 and 1 atm. To this end, in-situ XRD analysis coupled with Rietveld refinement has been performed. Additional TG analysis of calcination under similar conditions was carried out, which has been useful also to accurately measure in-situ the carbonation reactivity of the CaO stemming as final product of decomposition. Further tests on limestone decomposition under the same conditions have been performed whose results highlight the distinct role of the presence of CO_2 on decomposition of both materials.

III. MATERIALS AND METHODS

In our study we have used a powdered natural dolomite from Bueres quarry (Asturias, Spain). Raw dolomite was sieved (opening size 45 μm) in order to avoid decrepitation phenomena during thermal decomposition, which may be significant for particles of size above $\sim$ 100 μm as reported elsewhere [31, 35]. The average particle size of the sieved powder is $d_p \simeq$35 μm (volume weighted mean) as measured using a Malvern Mastersizer 2000 instrument by laser diffractometry. Such small particle size allows us also neglecting intra-particle diffusion resistance effects on the reaction rate that would be relevant only for particles of size larger than 300 μm [36, 37]. The major mineral phase identified by XRD analysis at ambient temperature is $CaMg(CO_3)_2$ (dolomite) with a minor $CaCO_3$ calcite phase. Phase quantification by Rietveld refinement yields a 94.4wt% of dolomite (SD=0.3%) the rest being calcite. For comparison, some experiments were carried out using a natural limestone of high purity (99.6wt% $CaCO_3$) from Matagallar quarry (Pedrera, Spain) with average particle size of 9.5 μm.

TGA tests were performed using a Q5000IR TG analyzer (TA Instruments) equipped with

a high sensitivity balance (<0.1 μg) characterized by a minimum baseline dynamic drift (<10 μg). Samples of small and fixed mass (10 mg) were tested in order to avoid undesired effects due to CO_2 diffusion resistance through the powder bulk, which would become relevant in this type of analysis for sample masses above ∼40 mg [38]. Heat transfer phenomena is also minimized by placing the sample inside a SiC enclosure heated by four symmetrically placed IR halogen lamps, which ensures consistent and uniform heating. Active water-cooling of the surrounding furnace body provides an efficient heat-sink and favors accurate temperature and heating rate control. The temperature is registered by a thermocouple positioned underneath and close to the sample. Quick heating of the gas up to the desired temperature is achieved by using a small gas flow rate (100 cm^3min^{-1}). At this small flow rate the gas velocity has no influence on the reaction rate [39]. In the tests reported in the present study, the sample is subjected to a N_2/CO_2 controlled gas mixture at atmospheric pressure and the temperature is increased from ambient temperature at 10°C/min up to the target calcination temperature, which is kept constant for 1h, after which the temperature is quickly decreased down to 650°C (300°C/min rate) and the sample is subjected to a gas mixture of 15%CO_2/85%N_2 vol/vol (typical ratio of post-combustion flue gas) in order to test in-situ the carbonation reactivity of the CaO product that results immediately after calcination.

In-situ XRD analysis has been carried out using a powder diffractometer (Bruker D8 Advance) equipped with a high temperature chamber (Anton Paar XRK 900) and a fast response/high sensitivity detector (Bruker Vantec 1) with radial Soller slits, which allows us investigating the evolution of the solid crystal structure as calcination progresses. The reactor chamber is specifically designed to ensure its homogeneous filling with the reaction gas at the desired temperature and avoid temperature gradients across the sample in order

to specifically study gas-solid reactions up to high temperatures. Reliable measurement and control of temperature is carried out by means of NiCr/NiAl thermocouples placed near the sample holder. 60 mm Gobel mirrors (Bruker) were employed for Cu K_α radiation (0.15405 nm wavelength) with parallel Johansson geometry in the incident beam. Instrumental contribution for structural adjustments was carried out in a wide range of diffraction angles using corundum, LaB_6 and silicon standards. Each test is started by placing the powder sample (of mass around 150 mg) over a 1 cm diameter porous ceramic plate. The N_2/CO_2 controlled gas mixture at atmospheric pressure is passed directly across the powder in the gravity direction at a small flow rate (100 cm^3/min). In this way, the gas is evenly distributed through the powder, which enhances the gas-solid contacting efficiency thus minimizing undesired effects caused by inefficient mass and heat transfer on the reaction rate that would arise for such a relatively big mass if the gas flow were passed over the sample as in TGA tests. The temperature during in-situ XRD experiments is increased at a rate of 10°C/min from ambient up to 925°C. XRD scans of duration $\Delta t = 295$ s are registered in the range $20° < 2\theta < 60°$ (0.03°/step) each 25°C at constant temperature from $T = 400$°C, after which the temperature is held constant at 925°C while XRD scans are continuously recorded for 1 h.

IV. SEM/PHYSISORPTION ANALYSES

Figure 1 illustrates scanning electron microscopy (SEM) images of dolomite samples calcined in atmospheres of pure N_2 and CO_2, respectively. It is clear from this micrographs that the presence of CO_2 in the calcination environment enhances sintering of both the MgO and CaO grains, which appear as well more segregated for the sample calcined under CO_2. Figure 2 shows the pore size distribution of the dolomite samples calcined under diverse

CO_2 partial pressures (obtained by N_2 physisorption analysis at 77 K). As inferred from SEM observations, calcination under CO_2 yields a much less porous structure as compared to N_2 calcination leading to a great reduction of BET surface area, which is 28.2 m^2/g for the sample calcined under N_2 and just 4.8 m^2/g for the sample calcined in a pure CO_2 environment. Remarkably, the effect of calcining under CO_2 on the pore size distribution is not linear with the CO_2 partial pressure and even at relatively low values of CO_2 concentration there is a drastic reduction of porosity. The enhancement of sintering that causes the presence of CO_2 in the calcination atmosphere has been already observed in the past from specific surface area measurements of CaO samples derived from limestone calcination [40]. Figure 1 shows that sintering of MgO grains durig dolomite calcination under CO_2 is also enhanced. A relevant but still unsolved question is what is the link between the mechanism of decomposition and the accelerated sintering under CO_2 as we see also in our study for the dolomite samples too, which causes a drastic reduction of the CaO reactivity towards carbonation as will be shown. Our experimental work described below is aimed at shedding light on this issue.

V. THERMOGRAVIMETRIC ANALYSIS

A. Thermal decomposition

The thermograms displayed in Figs. 3-4 show the time evolution of sample weight and its time derivative during decomposition of dolomite and limestone tested by TGA (high degree of repeatability was checked from several measurements on diverse samples at same conditions). As seen in Fig. 3a, the weight loss that takes place during decomposition of dolomite and limestone samples under pure N_2 follow practically identical trends. It

starts to be noticeable at $T \simeq$550°C and ends up at around 750°C. In contrast, calcination of both materials under CO_2 (Fig. 3b) occurs along rather different paths. The onset of limestone decomposition under pure CO_2 is delayed up to $T \simeq 925$°C, which is well over the equilibrium temperature ($T_{eq} \simeq 895$°C under pure CO_2 at atmospheric pressure according to Eq. 4). As shown in previous works, the presence of CO_2 at high partial pressure in the calciner environment hinders notably the calcination of limestone, which takes place quickly only at temperatures about 30°C above the equilibrium calcination temperature [7, 8, 41]. On the other hand, Fig. 3b shows that dolomite undergoes decomposition under CO_2 through two well differentiated stages as widely reported in the literature [4, 22–24]. The first stage is initiated around $T \simeq 700$°C and finishes at around 800°C. According to the weight loss observed, the main products of the first decomposition stage under CO_2 would be MgO and $CaCO_3$ in agreement with reaction 2. A second decomposition stage that would obey to $CaCO_3$ decarbonation is started at a slightly lower temperature as compared to limestone. Interestingly, a small and reproducible loss of weight is observed (both during limestone and dolomite decomposition) at $T \simeq 900$°C (see Fig. 3b), which is close to the equilibrium temperature for $CaCO_3$ calcination albeit the weight is immediately recovered afterwards. We made several tests under the same conditions and this transitory weight drop was systematically observed.

Let us now discuss further the effect of the CO_2 partial pressure P in the calcination environment on the weight loss evolution during dolomite decomposition. As can be seen in Figs. 3-4, the temperature at which the first stage of decomposition occurs is not essentially affected by P. In contrast, the second stage is anticipated to smaller temperatures as P is decreased in qualitative accordance with the variation of the equilibrium temperature for $CaCO_3$ calcination with P (T_{eq} in Eq. 4). Remarkably, the rate of $CaCO_3$ decomposition is

decreased as the CO_2 partial pressure is lowered down, which indicates that decarbonation takes place at temperatures closer to the equilibrium temperature T_{eq} as P is decreased. Thus, the second decomposition stage under 25%CO_2/75%N_2 ($P = 0.25$ atm) is observed to occur at temperatures between 800 and 850°C, which are close to the equilibrium temperature for $CaCO_3$ calcination ($T_{eq} \simeq 810$°C according to Eq. 4). On the other hand, the 2nd decomposition stage under pure CO_2 ($P = 1$ atm) takes place at temperatures between 920 and 950°C, which are well over the equilibrium temperature ($T_{eq} \simeq 895$°C). Figure 4 shows a comparison on how a change of the CO_2 partial pressure affects decomposition of $CaCO_3$ for dolomite (2nd decomposition) and limestone. It may be observed that $CaCO_3$ decomposition is further hindered for limestone and occurs at temperatures 10-15°C higher than for $CaCO_3$ derived from half-decomposition in dolomite. As seen in previous studies [7, 41, 42], limestone calcination in the presence of CO_2 in the calcination environment is notably hampered by CO_2 desorption and the structural transformation of a metastable CaO^* form to the stable CaO crystal structure. Arguably, this transformation may occur more easily for the $CaCO_3$ that stems from dolomite 1st decomposition.

B. CaO carbonation reactivity

TGA runs were concluded by an in-situ CaO carbonation stage carried out immediately after calcination. To this end, the calcined samples were subjected to a 15%CO_2/85%N_2 vol/vol mixture gas flow at atmospheric pressure and the temperature was quickly decreased (300°C/min) down to 650°C (typical CaL conditions for post-combustion CO_2 capture). At these conditions, MgO carbonation is not thermodynamically favorable and therefore MgO grains remain inert. Figure 5 illustrates the time evolution of CaO conversion $X(t)$ (ratio of grams of CaO carbonated to grams of CaO initial). Basically, carbonation of the CaO

grains occurs through two well-differentiated stages as well known from previous studies [37, 43, 44]. After a very short nucleation period of just a few seconds, carbonation enters a relatively fast reaction-controlled regime that takes place at the surface of the particles until a 30-50 nm layer of carbonate is built up [37, 43, 44]. Once the reaction-controlled phase is ended, carbonation becomes limited by the counter-current diffusion of CO_3^{2-} inward and O^{2-} outward through the carbonate layer, which slows down CaO conversion [37, 43, 45]. As may be seen in Fig. 5, CaO conversion increases roughly linearly with time in the reaction-controlled regime until it reaches a certain value X_r, after which it evolves at a slower rate as it turns to be controlled by solid-state diffusion.

Figure 5 demonstrates a remarkable dependence of the rate of CaO conversion on both the CaO precursor type (either dolomite or limestone) and the presence of CO_2 in the calcination environment. The rate of CaO conversion is substantially higher both in the reaction and solid-state diffusion controlled regimes for dolomitic CaO in the presence of CO_2 as compared to N_2 (Fig. 5) whereas it is otherwise for limestone derived CaO whose reactivity towards carbonation is severely hindered when calcination is carried out under high CO_2 partial pressure. As can be seen, the maximum conversion in the reaction-controlled phase X_r is notably higher for CO_2-calcined dolomite as compared to limestone (see inset of Fig. 5), which indicates that the surface area available for reaction-controlled carbonation is promoted in calcined dolomite as compared to limestone. Note also that the enhancement of solid-state diffusion controlled carbonation in dolomitic CaO cannot be attributed to the presence of inert MgO grains as demonstrated by the results obtained for N_2-calcined dolomite showing no enhancement of diffusion controlled carbonation. Instead the time evolution of conversion for N_2-calcined dolomite resembles the behavior of limestone derived CaO (Fig. 5b) albeit CaO conversion in the kinetically controlled regime reaches a higher

value, which is indicative of a less degree of CaO sintering. Thus, the presence of CO_2 is also essential for promoted CaO carbonation in dolomite specially in the diffusion controlled regime. It may be argued that the transient formation of $CaCO_3$ by carbonation of CaO that would stem as a direct product of dolomite half-decomposition plays a determining role on this behavior. Thus, the subsequent decarbonation of the intermediate $CaCO_3$ would lead to a CaO structure with promoted reactivity towards carbonation. A goal of the XRD in-situ analysis described below is to investigate the validity of this argument.

VI. IN-SITU XRD ANALYSIS

A. Evolution of Phases

Figures 6a-b show the XR diffractograms registered during calcination tests of dolomite under CO_2 and N_2, respectively. As inferred from TGA tests, the evolution with temperature of the Bragg reflection peaks of the different phases involved in the reaction indicate that calcination under CO_2 occurs through two well differentiated stages at temperatures similar to those inferred from the TG analysis. The main products of half-decomposition are calcite ($CaCO_3$) and periclase (MgO), whose reflection peaks are firstly observed in the scan recorded at 725°C. Later on, calcite decomposes into lime (CaO) whose reflection peaks are first seen at 925°C. This second decomposition stage occurs rather fast as seen from the subsequent scans recorded at 925°C and in accordance with the TG study. In agreement with previous works [27, 46], Bragg reflection peaks that would correspond to magnesite ($MgCO_3$) do not appear in the diffractograms, which sheds doubts on the validity of a reaction mechanism based on the decomposition of dolomite into the two carbonates (Eq. 5) at least at the calcination conditions of our tests and assuming that these phases are not

amorphous or very poorly crystalline as not to yield visible diffraction peaks. It becomes also apparent from the breadths of Bragg reflection peaks that the coherent crystal length (crystallite size) of the final CaO and MgO products is larger when dolomite is calcined under CO_2. The results of a quantitative analysis on this issue will be shown below.

XR diffractograms obtained for dolomite and limestone samples calcined in pure CO_2 immediately at the end of the temperature ramp ($T = 925°C$) and after 1h at 925°C are superposed in Fig. 7. The notably less sharpness of the reflection peaks for calcite and lime obtained from dolomite (Fig. 7a) reveals a lower degree of crystallinity for these products of decomposition. Another interesting feature illustrated in the inset of Fig. 7b is that the peaks of the CaO phase obtained from dolomite decomposition are slightly shifted with respect to the peaks obtained for CaO derived from decomposition of limestone. As will be seen, a Rietveld refinement analysis suggests that this relative displacement is possibly caused by the presence of Mg impurities in the structure of CaO derived from dolomite.

A quantitative phase analysis of the registered XRD scans has been carried out by means of the Rietveld method [47] and using the software TOPAS 4.2 (Bruker) [48]. Zero error (2θ), sample displacement, absorption (1/cm), lattice parameters of the phases as well as site occupancy of Mg impurities in calcite and lime and Ca impurities in periclase were allowed to vary to provide the best fits to the experimental diffractograms. Dilation of the structure as affected by temperature is also considered in the analysis. The background was fitted by a fourth-order Chebychev polynomial. Lorentz and polarization geometric factors for the measurement configuration were used. For the fittings to be as accurate as possible the resulting value of the GOF (Goodness-of-fit) parameter should be above unity and as close as possible to it [47]. Furthermore, the residual factors (Rwp and RBragg) have to be small for the measurement configuration used [47]. In general, acceptable fitting indicators

were obtained in our analysis (GOF ∼1-1.5, Rwp∼ 10, RBragg∼1).

The evolution with temperature of the wt% for the $CaMg(CO_3)_2$ and MgO phases during dolomite decomposition as depending on the CO_2 vol% in the calcination environment is shown in Fig. 8. As may be seen, the drop of $CaMg(CO_3)_2$ wt% is accompanied by a increase of the wt% of MgO that stems as a direct product of half decomposition and remains inert to the presence of CO_2. In accordance with the TGA results, dolomite decomposition is started in the absence of CO_2 at relatively lower temperatures whereas there is not a remarkable dependence of the decomposition temperature on the concentration of CO_2 present. Figure 9 shows a comparison of the evolution with temperature of $CaCO_3$ and CaO wt% for dolomite calcination under pure CO_2 (Fig. 9a) and pure N_2 (Fig. 9b). Note that the small amount of $CaCO_3$ prior to half-decomposition (about 6%) is due to calcite originally present in the dolomite samples. Half-decomposition, as inferred from the emergence of MgO Bragg reflection peaks, is initiated at 700°C for decomposition under CO_2 and at 650°C in the case of decomposition under N_2. As seen in Fig. 9a half-decomposition under CO_2 leads to a remarkable rise of the $CaCO_3$ wt% that results as a product of decomposition together with MgO. On the other hand, the products of half-decomposition under N_2 are MgO and CaO while the $CaCO_3$ initially present in the sample drops abruptly to zero as decarbonation of calcite at the temperature of decomposition becomes thermodynamically favorable and fast under N_2.

Interestingly, it is seen in Figs. 9a-9b that, after the initiation of decomposition, the $CaCO_3$ and CaO wt% for calcination under CO_2 and N_2, respectively, follow comparable trends reaching both a similar maximum value (around 63%) at the same temperature (750°C). This observation suggests that the mechanism that rules dolomite decomposition in both cases basically consists of the direct breakdown of the dolomite structure into MgO and

CaO with the immediate recarbonation of the nascent CaO crystals when calcination is carried out under CO_2. Thus, CaO would remain carbonated under CO_2 until the temperature reaches a sufficiently high value for decarbonation to be thermodynamically favorable and fast enough. As seen in Fig. 9a this occurs for temperatures above 925°C when calcination is carried out under pure CO_2. Remarkably, best Rietveld fittings for decomposition under CO_2 suggest that the product of the reaction is pure calcite without Mg impurities. This contrasts with previous ex-situ XR studies indicating the formation of Mg-calcite [27] or a solid solution of MgO in calcite [3]. It is also noticeable that, for decomposition under N_2, MgO and CaO reflection peaks start to become visible at a temperature (650°C) which is roughly 100°C over the temperature at which TGA tests indicate the initiation of weight loss (Fig. 3a). This suggests that the nascent oxides are poorly crystalline or even amorphous as inferred from other works [27]. In contrast, for decomposition under CO_2, MgO reflection peaks and the intensification of calcite peaks occur at a temperature (700°C) close to that at which weight loss is started according to TGA results (Fig. 3a), which indicates that the nascent oxides are already in a well defined crystalline form if decomposition takes place under CO_2.

Taking into account the presence of $CaCO_3$ by a small amount ($\simeq 6\%$) initially in the dolomite powder, the theoretical wt% for the final CaO and MgO products after decomposition would be close to 39% and 61%, respectively if pure CaO/MgO phases are assumed. On the other hand, the Rietveld analysis reveals that the wt% of CaO and MgO in the fully decomposed samples after the 1h isotherm at 925°C are in the ranges 37-38% and 62-63%, respectively. This slight difference between the expected and obtained wt% can be explained from the presence of Mg impurities in the CaO structure. Figure 10 illustrates an example of the best Rietveld fits to the XRD pattern measured for dolomite decomposition

in pure CO_2 (1h at 925°C after the end of the temperature ramp) either assuming pure CaO and MgO phases (Fig. 10a) or allowing for the presence of Ca and Mg impurities in the MgO and CaO phases, respectively. A considerably better fit is obtained in the latter case (fitting indicators are given in the figure caption). Thus, the shift of the CaO peaks with respect to the peaks of pure CaO derived from limestone above observed (inset of Fig. 7b) can be accounted for by allowing a certain occupation of Mg atoms in the CaO structure. Arguably, the presence of Mg impurities in CaO could contribute to the enhancement of the solid-state diffusion controlled carbonation of dolomitic CaO inferred from the TGA tests. On the other hand, best Rietveld fits indicate that the MgO phase does not contain Ca impurities.

B. Evolution of Crystallite Size

Crystallite size for the main phases involved in dolomite decomposition (dolomite $CaMg(CO_3)_2$, calcite $CaCO_3$, lime CaO and periclase MgO) has been calculated from the XR patterns by means of the Le Bail method [49] and using the software TOPAS 4.2 (Bruker) [48]. Data are plotted in Fig. 11 as depending on the CO_2 vol% in the calcination atmosphere. Generally, the values obtained for the fitting indicators such as the GOF and residual factors (Rwp and RBragg) are indicative of reliable results (GOF$\sim$1-1.5, Rwp$\leq$8, RBragg$\leq$0.5) [47]. Data reproducibility is demonstrated in Fig. 11a, where the evolution of crystallite size with temperature is plotted for independent calcination tests carried out under CO_2 and using diverse samples. Data on CaO and MgO crystallite size are consistent in order of magnitude with data reported elsewhere from ex-situ XR analysis [27, 50].

An interesting advantage of the in-situ XR analysis over ex-situ studies is that it yields noninvasively the evolution of crystallite size during calcination. As may be seen in Fig. 11b,

$CaMg(CO_3)_2$ crystallite size remains roughly constant independently of the CO_2 partial pressure before decomposition. Only when the temperature approaches $T \simeq 700°C$, the crystallite size of $CaMg(CO_3)_2$ declines as its reflection peaks disappear and calcite (or CaO under N_2) and MgO reflection peaks start to emerge. As temperature is increased above 700°C, $CaCO_3$ crystallite size, which may be accurately measured in the interval between 700 and 925°C for decomposition under pure CO_2, grows with temperature similarly to CaO and MgO crystallite size. This result is consistent with the argument that the direct products of dolomite decomposition are MgO and CaO, the latter being immediately carbonated when calcination is carried out under high CO_2 concentration. It can be noticed also that the size of CaO crystallites, which emerge at 925°C for calcination under pure CO_2 (Fig. 11c), is larger than that of the CaO crystallites that emerged at 700°C for calcination at lower CO_2 concentrations. As demonstrated from dolomite calcination under vacuum by in-situ TEM [27], the nascent crystals would grow by oriented aggregation and sintering. Initially, attractive forces between the nanosized crystals due to the universal van der Waals interaction would lead to their aggregation. Since these attractive forces are enhanced by the presence of adsorbed CO_2 molecules [51] on the solid surfaces, crystal coarsening would be expectedly promoted when calcination is carried out under high CO_2 partial pressure. Accordingly, it can be seen in Fig. 11 that the rate of growth of CaO and MgO crystals with temperature is notably increased with the concentration of CO_2 in the calcination environment.

Figure 12 shows data on the size of CaO and MgO crystallites calculated from the in-situ XRD patterns registered during the 1 h isotherm at 925°C. As can be observed, the size of the crystallites is only slightly increased with time regardless of the CO_2 concentration in the calcination atmosphere. Thus, the final size of crystallites is mainly determined

by their growth during the temperature ramp. Crystallite coarsening at 925°C far from the equilibrium temperature would be mainly driven by sintering [41], which essentially depends on the Tamman temperature. The Tammann temperature of a ceramic material (T_t) marks the initiation of notable sintering by diffusion of chemical species across the crystalline lattice and corresponds to about half the melting temperature in K ($T_t \simeq 1170$°C for CaO and $T_t \simeq 1276$°C for MgO) [52, 53]. At lower temperatures, as in the present case, sintering would be governed by surface diffusion albeit lattice diffusion could be promoted by the presence of defects and impurities in the crystal structure [54]. Our results indicate that the major influence of CO_2 on the growth of CaO and MgO crystallites stemming from dolomite decomposition is attributable to the promotion of nanosized crystal aggregation in the initial nucleation phase. Note also that the rate of growth of crystallite size is similar for both CaO and MgO.

The evolution of calcite and CaO crystallite size during calcination of dolomite under pure CO_2 is shown in Fig. 13(a-b) in comparison to data obtained for calcination of limestone under the same conditions. Note that the size of $CaCO_3$ crystallites in limestone before decomposition ($L \sim 100$ nm) is comparable to the size of dolomite crystallites before decomposition (Fig. 11a). On the other hand, $CaCO_3$ crystallites that nucleate after half-decomposition of dolomite are notably smaller ($L \sim 50$ nm) and increase in size with temperature as discussed above. CaO appears first for decomposition of both materials at 925°C with a similar crystallite size ($L \sim 50$ nm). However, the crystallites of CaO derived from limestone experience a marked increase during the initial stages of calcination at 925°C up to reach a value of around 100 nm whereas the growth of CaO crystallites for dolomite is hindered (Fig. 11b). The enhanced growth of CaO crystallites during limestone calcination would be arguably caused by aggregation of the nascent CaO nanocrystals due to surface

attractive forces between them [41]. Presumably, these short ranged van der Waals forces would be mitigated in the case of dolomite (as compared to limestone) by the interposition of MgO grains in between the CaO nanocrystals. It is also noticeable that the size of dolomite derived $CaCO_3$ crystallites is, at the end of the temperature ramp, $L \simeq 70 - 80$ nm (Fig. 13a) which is considerably smaller than the size of $CaCO_3$ crystallites in the natural limestone before decomposition ($L \simeq 100 - 120$ nm, Fig. 13a). This would explain why decarbonation of $CaCO_3$ in the second decomposition stage of dolomite occurs at lower temperatures than $CaCO_3$ decomposition in limestone as seen above from the TGA tests (Fig. 3). An analogous effect is seen when limestone is mechanically milled, which reduces the size of $CaCO_3$ crystallites [55]. Generally, a decrease of the crystallite size leads to a higher reactivity of the material, which reduces the nucleation period that usually precedes gas-solid reactions and accelerates decomposition [41]. Data on the size of CaO crystallites obtained from decomposition of both materials under N_2 are plotted in Fig. 13(c-d). As seen for decomposition under CO_2, the crystallinity of CaO derived from dolomite is considerably reduced as compared to limestone derived CaO.

VII. CRYSTAL STRUCTURE, SINTERING AND CAO REACTIVITY

Previous works on limestone decomposition [8, 40, 56] demonstrate that the enhanced growth of CaO crystallite size when calcination is carried out at high temperatures and high CO_2 partial pressure leads to a marked decrease of the CaO surface area which would be available for reaction-controlled carbonation. Thus, the notably smaller size of CaO crystallites stemming from dolomite decomposition would explain their higher reactivity towards carbonation demonstrated by the TGA results above shown (Fig. 5) as compared to the carbonation reactivity of CaO obtained from limestone. Figure 14a shows that the final

size of CaO and MgO crystallites derived from dolomite decomposition is correlated to the BET surface area S measured for the calcined samples according to a power law $L \propto S^{\lambda}$ with a similar exponent $\lambda \sim -0.5$ for both CaO and MgO. This result questions the generally accepted role of MgO as a *thermally stable* support to mitigate CaO sintering during multiple calcination/carbonation cycles of dolomite [53]. Dolomite samples subjected to calcination/carbonation cycles exhibit sintering of the CaO grains and decay of CaO carbonation reactivity as the $CaCO_3$/CaO transformation is repeated in each cycle. As CaO grains, MgO grains suffer significant sintering during decomposition as observed in the SEM pictures of the calcined samples (Fig. 1). Yet, MgO grains are inert during subsequent calcination/carbonation cycles and their size remain essentially unchanged [17]. It may be thus argued that, according to our results, most of CaO sintering would occur along multiple calcination/carbonation cycles by enhanced aggregation during the $CaCO_3$/CaO transformation, which would be enhanced by the presence of CO_2 in the calcination environment at high partial pressure. The main effect of the inert MgO grains would be thus to reduce surface forces between the nascent CaO crystals, which would mitigate subsequent CaO sintering in each calcination stage. As seen in Fig. 14b, CaO conversion in the kinetically controlled phase X_r scales proportionally to the BET surface area for CaO derived from dolomite calcination under diverse CO_2 partial pressures, which leads to a very low particle porosity and small surface area ($S < 10$ m^2/g). On the other hand, conversion of CaO derived from the sample calcined under N_2 and with a relatively higher porosity, is lower than expected from this linear law ($X_r \simeq 0.56$ for $S \simeq 28$ m^2/g). In this case, a further limiting factor for fast carbonation would be the diffusion of CO_2 through the pores of the particles [57].

VIII. CONCLUSIONS

A main conclusion of the present work is that the fundamental mechanism of dolomite decomposition under CO_2 determines essentially the carbonation reactivity of the generated CaO. Our results indicate that dolomite suffers a direct breakdown into MgO ad CaO at temperatures around 700°C while the nascent CaO crystals are immediately carbonated. $CaCO_3$ remains stable until a temperature is reached for decarbonation to be thermodynamically favorable and sufficiently fast, which depends on the CO_2 partial pressure in the calcination environment. $CaCO_3$ crystallites derived from this carbonation have a small size as compared to $CaCO_3$ crystallites in limestone, which explains their higher reactivity towards decarbonation. Thus, the $CaCO_3$/CaO transformation occurs at lower temperatures for dolomite. This behavior may be useful for applications requiring the generation of CaO by calcination under CO_2 such as the Calcium-Looping technology for CO_2 capture or in-situ SO_2 removal in oxy-combustion reactors. The use of dolomite instead of limestone in the CaL technology as CaO precursor would allow reducing the calcination temperature thus minimizing the energy penalty. Moreover, the CaO resulting from dolomite decomposition show a substantially higher reactivity towards carbonation as compared to limestone derived CaO. CaO reactivity in the reaction controlled phase is directly correlated to CaO crystallite size. A further important observation in our work is that carbonation reactivity in the solid-state diffusion controlled phase is remarkably enhanced for CaO derived from dolomite in the presence of CO_2. The use of dolomite would therefore allow increasing significantly the carbonation efficiency by prolonging the residence time of the solids in the carbonator reactor.

IX. ACKNOWLEDGEMENTS

This work was supported by the Spanish Government Agency Ministerio de Economia y Competitividad (contracts CTQ2014-52763-C2-1-R and CTQ2014-52763-C2-2-R) and Andalusian Regional Government Junta de Andalucia (contract FQM-5735). We gratefully acknowledge the X-ray service of the Innovation, Technology and Research Center of the University of Seville (CITIUS).

---

[1] Seeley, N. J. *Journal of Architectural Conservation* **2000,** *6,* 21 - 29.

[2] Beruto, D.; Vecchiattini, R.; Giordani, M. *Thermochimica Acta* **2003,** *404,* 25–33.

[3] Beruto, D.; Vecchiattini, R.; Giordani, M. *Thermochimica Acta* **2003,** *405,* 183 - 194.

[4] Caceres, P.; Attiogbe, E. *Minerals Engineering* **1997,** *10,* 1165 - 1176.

[5] O'Neill, E.; Keairns, D.; Kittle, W. *Thermochimica Acta* **1976,** *14,* 209 - 220.

[6] Ulerich, N.; O'Neill, E.; Keairns, D. *Thermochimica Acta* **1978,** *26,* 269 - 282.

[7] Hyatt, E. P.; Cutler, I. B.; Wadsworth, M. E. *Journal of the American Ceramic Society* **1958,** *41,* 70–74.

[8] Valverde, J. M.; Sanchez-Jimenez, P. E.; Perez-Maqueda, L. A. *The Journal of Physical Chemistry C* **2015,** *119,* 1623-1641.

[9] Garca-Labiano, F.; Rufas, A.; de Diego, L. F.; de las Obras-Loscertales, M.; Gayn, P.; Abad, A.; Adanez, J. *Fuel* **2011,** *90,* 3100 - 3108.

[10] de Diego, L.; Rufas, A.; Garca-Labiano, F.; de las Obras-Loscertales, M.; Abad, A.; Gayn, P.; Adanez, J. *Fuel* **2013,** *114,* 106 - 113.

[11] Shimizu, T.; Hirama, T.; Hosoda, H.; Kitano, K.; Inagaki, M.; Tejima, K. *Chemical Engineering Research & Design* **1999,** *77,* 62 - 68.

[12] Arias, B.; Diego, M.; Abanades, J.; Lorenzo, M.; Diaz, L.; Martinez, D.; Alvarez, J.; Sanchez-Biezma, A. *International Journal of Greenhouse Gas Control* **2013,** *18,* 237–245.

[13] Ströhle, J.; Junk, M.; Kremer, J.; Galloy, A.; Epple, B. *Fuel* **2014,** *127,* 13 - 22 Fluidized Bed Combustion and Gasification CO2 and SO2 capture: Special Issue in Honor of Professor E.J. (Ben) Anthony.

[14] Martinez, I.; Grasa, G.; Murillo, R.; Arias, B.; Abanades, J. *Chemical Engineering Journal* **2013,** *215–216,* 174–181.

[15] Martinez, A.; Lara, Y.; Lisbona, P.; Romeo, L. M. *International Journal of Greenhouse Gas Control* **2012,** *7,* 74 - 81.

[16] Charitos, A.; Rodriguez, N.; Hawthorne, C.; Alonso, M.; Zieba, M.; Arias, B.; Kopanakis, G.; Scheffknecht, G.; Abanades, J. C. *Industrial & Engineering Chemistry Research* **2011,** *50,* 9685–9695.

[17] Valverde, J.; Sanchez-Jimenez, P.; Perez-Maqueda, L. *Applied Energy* **2015,** *138,* 202 - 215.

[18] Silaban, A.; Narcida, M.; Harrison, D. P. *Chemical Engineering Communications* **1996,** *146,* 149–162.

[19] Albrecht, K. O.; Wagenbach, K. S.; Satrio, J. A.; Shanks, B. H.; Wheelock, T. D. *Ind. Eng. Chem. Res.* **2008,** *47,* 7841 7848.

[20] Sultan, D. S.; Muller, C. R.; Dennis, J. S. *Energy & Fuels* **2010,** *24,* 3687–3697.

[21] Yang, X.; Zhao, L.; Yang, S.; Xiao, Y. *Asia-Pacific Journal of Chemical Engineering* **2013,** *8,* 906–915.

[22] Haul, R. A. W.; Heystek, H. *American Mineralogist* **1952,** *37,* 166-179.

[23] Otsuka, R. *Thermochimica Acta* **1986,** *100,* 69 - 80.

[24] Wiedemann, H.-G.; Bayer, G. *Thermochimica Acta* **1987,** *121,* 479 - 485.

[25] Spinolo, G.; Anselmi-Tamburini, U. *The Journal of Physical Chemistry* **1989,** *93,* 6837 - 6843.

[26] Cater, E.; Buseck, P. R. *Ultramicroscopy* **1985,** *18,* 241 - 251.

[27] Rodriguez-Navarro, C.; Kudlacz, K.; E.Ruiz-Agudo, *American Mineralogist* **2012,** *97,* 38-51.

[28] Rrodriguez-Navarro, C.; Ruiz-Agudo, E.; Luque, A.; Navarro, A. B.; Ortega-Huertas, M. *American Mineralogist* **2009,** *94,* 578 593.

[29] Bradley, W.; Burst, J.; Graf, D. *American Mineralogist* **1953,** *38,* 207 217.

[30] Galai, H.; Pijolat, M.; Nahdi, K.; Trabelsi-Ayadi, M. *Solid State Ionics* **2007,** *178,* 1039 - 1047.

[31] Dollimore, D.; Dunn, J.; Lee, Y.; Penrod, B. *Thermochimica Acta* **1994,** *237,* 125 - 131.

[32] Samtani, M.; Skrzypczak-Janktun, E.; Dollimore, D.; Alexander, K. *Thermochimica Acta* **2001,** *367–368,* 297 - 309.

[33] Arai, Y. *Chemistry of Powder Production;* Particle Technology Series Springer: Netherlands, 1996.

[34] Hashimoto, H.; Komaki, E.; Hayashi, F.; Uematsu, T. *Journal of Solid State Chemistry* **1980,** *33,* 181 - 188.

[35] McCauley, R.; Johnson, L. *Thermochimica Acta* **1991,** *185,* 271 - 282.

[36] Garcia-Labiano, F.; Abad, A.; de Diego, L.; Gayan, P.; Adanez, J. *Chemical Engineering Science* **2002,** *57,* 2381 - 2393.

[37] Grasa, G.; Murillo, R.; Alonso, M.; Abanades, J. C. *AIChE J.* **2009,** *55,* 1246–1255.

[38] Koga, N.; Criado, J. M. *Int. J. Chem. Kinet.* **1998,** *30,* 737-744.

[39] Alonso, M.; Criado, Y.; Abanades, J.; Grasa, G. *Fuel* **2014,** *127,* 52-61.

[40] Borgwardt, R. H. *Industrial & Engineering Chemistry Research* **1989,** *28,* 493 - 500.

[41] Valverde, J. M.; Medina, S. *Phys. Chem. Chem. Phys.* **2015,** *17,* 21912 - 21926.

[42] Valverde, J. M. *Chemical Engineering Science* **2015,** *132,* 169–177.

[43] Barker, R. *J. Appl. Chem. Biotechnol.* **1973,** *23,* 733 - 742.

[44] Bhatia, S. K.; Perlmutter, D. D. *AIChE Journal* **1983,** *29,* 79–86.

[45] Sun, Z.; Luo, S.; Qi, P.; Fan, L.-S. *Chemical Engineering Science* **2012,** *81,* 164 - 168.

[46] Engler, P.; Santana, M. W.; Mittleman, M. L.; Balazs, D. *Thermochimica Acta* **1989,** *140,* 67 - 76.

[47] Young, R. A., Ed.; *The Rietveld Method;* IUCr Monographs on Crystallography 5; Oxford University Press: New York, 1993.

[48] Bruker, A. *Bruker AXS GmbH, Karlsruhe, Germany Search PubMed* **2009,** .

[49] Le Bail, A. *Powder Diffraction* **2005,** *20,* 316–326.

[50] Haul, R. A. W.; Raal, F. A. *Zeitschrift fr anorganische und allgemeine Chemie* **1955,** *281,* 199–211.

[51] Xie, H.-Y.; Geldart, D. *Powder Technol.* **1995,** *82,* 269 – 277.

[52] Dollimore, D. *Journal of thermal analysis* **1992,** *38,* 111 - 130.

[53] Kierzkowska, A. M.; Pacciani, R.; Müller, C. R. *ChemSusChem* **2013,** *6,* 1130–1148.

[54] Borgwardt, R. H. *Chem. Eng. Sci.* **1989,** *44,* 53–60.

[55] Valverde, J. M.; Sanchez-Jimenez, P. E.; Perez-Maqueda, L. A. *Environmental Science & Technology* **2014,** *48,* 9882–9889.

[56] Stanmore, B.; Gilot, P. *Fuel Processing Technology* **2005,** *86,* 1707 - 1743.

[57] Alvarez, D.; Abanades, J. C. *Energy and Fuels* **2005,** *19,* 270–278.

X. REFERENCES

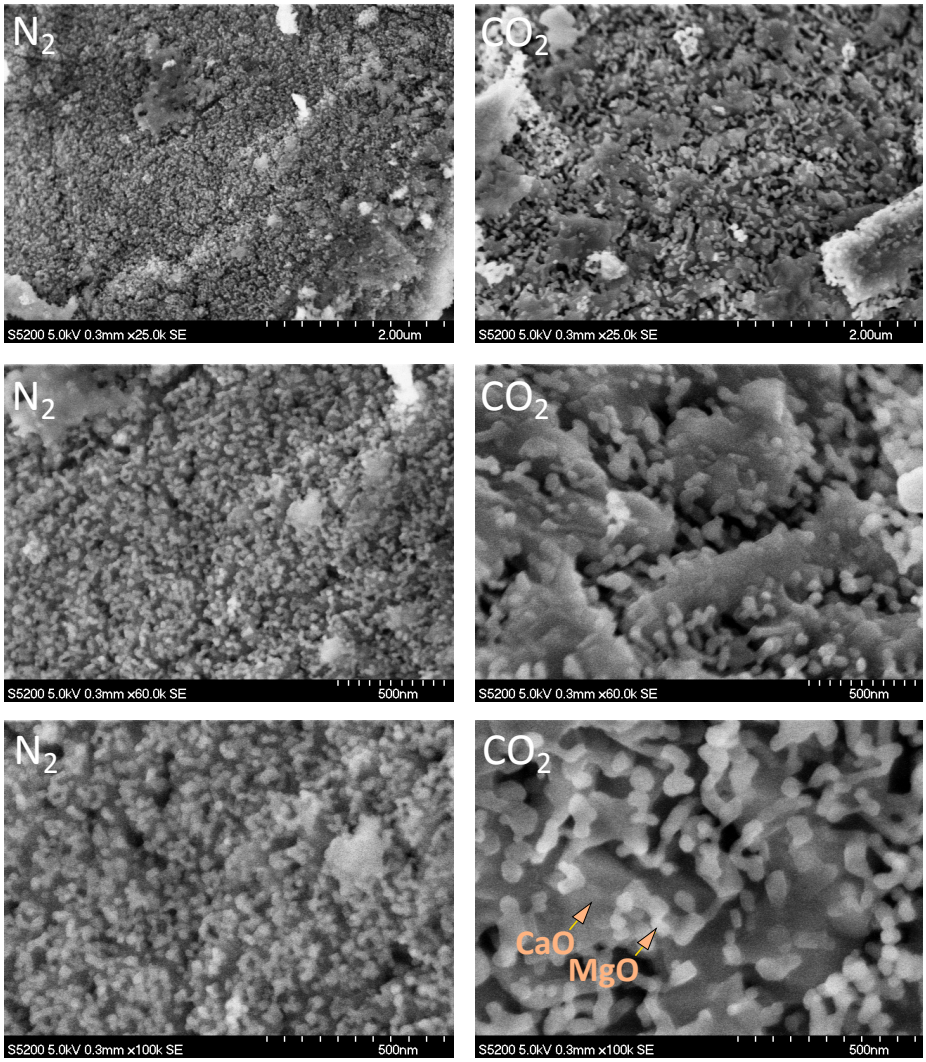

FIG. 1: SEM pictures of dolomite samples after being subjected to in-situ XRD calcination tests under N_2 (left) and CO_2 (right) atmospheres. CaO and MgO grains are indicated in the bottom-right picture.

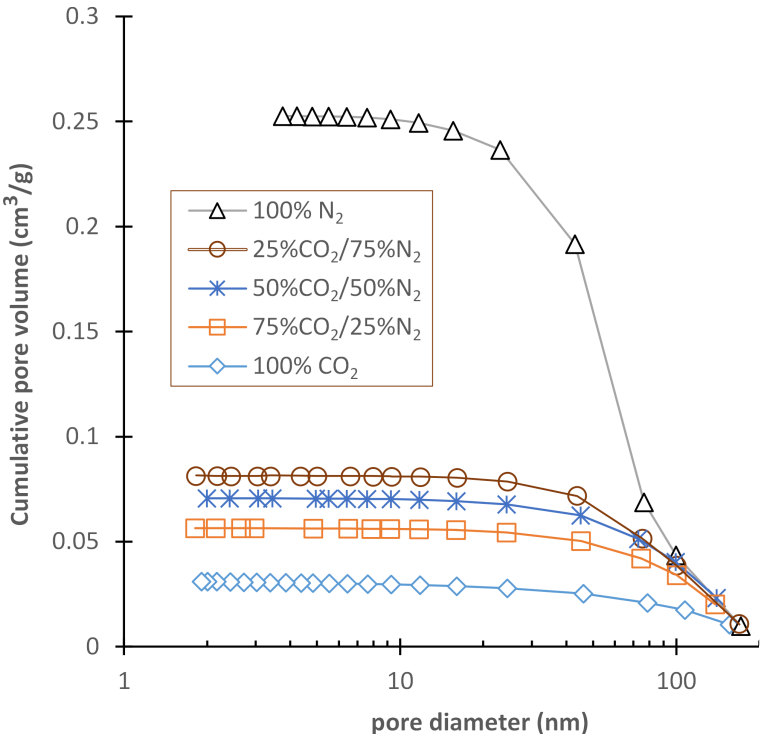

FIG. 2: BJH adsorption cumulative pore volume distribution as a function of pore diameter for the dolomite samples calcined during in-situ XRD tests under atmospheric pressure and diverse CO_2/N_2 volume concentrations as indicated.

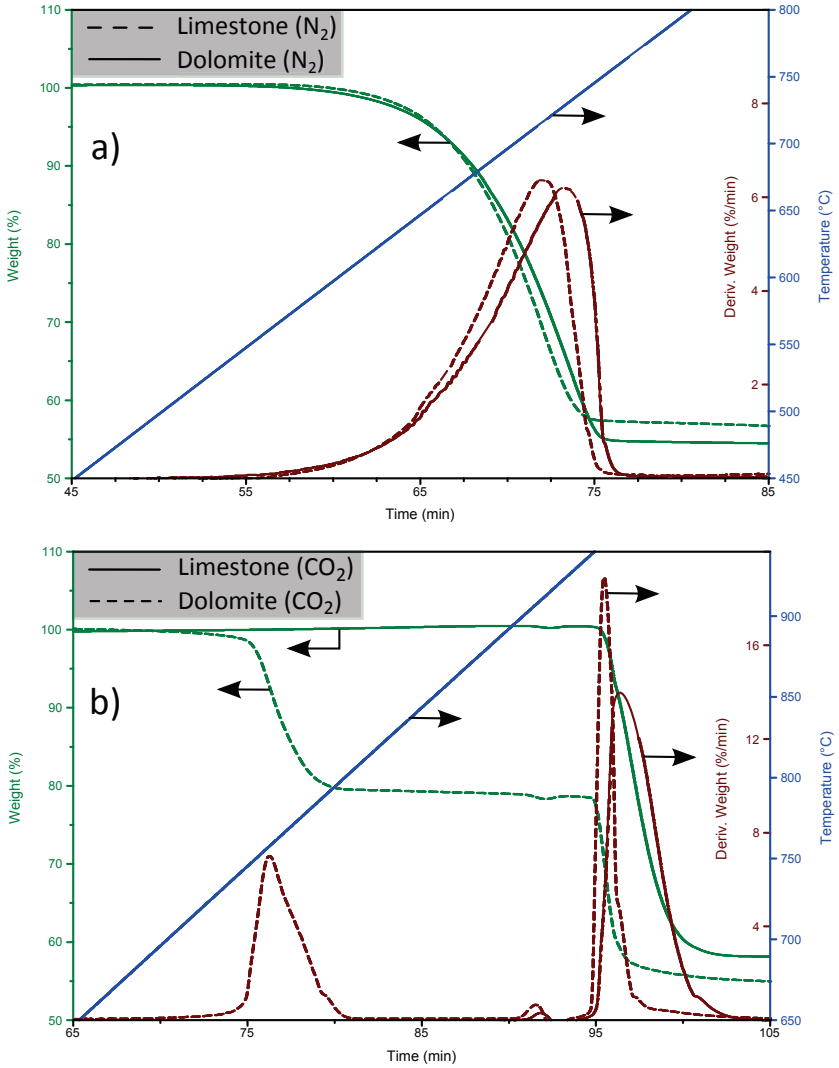

FIG. 3: Thermograms obtained for limestone and dolomite decomposition during calcination under pure N_2 (a) and CO_2 (b) at atmospheric pressure.

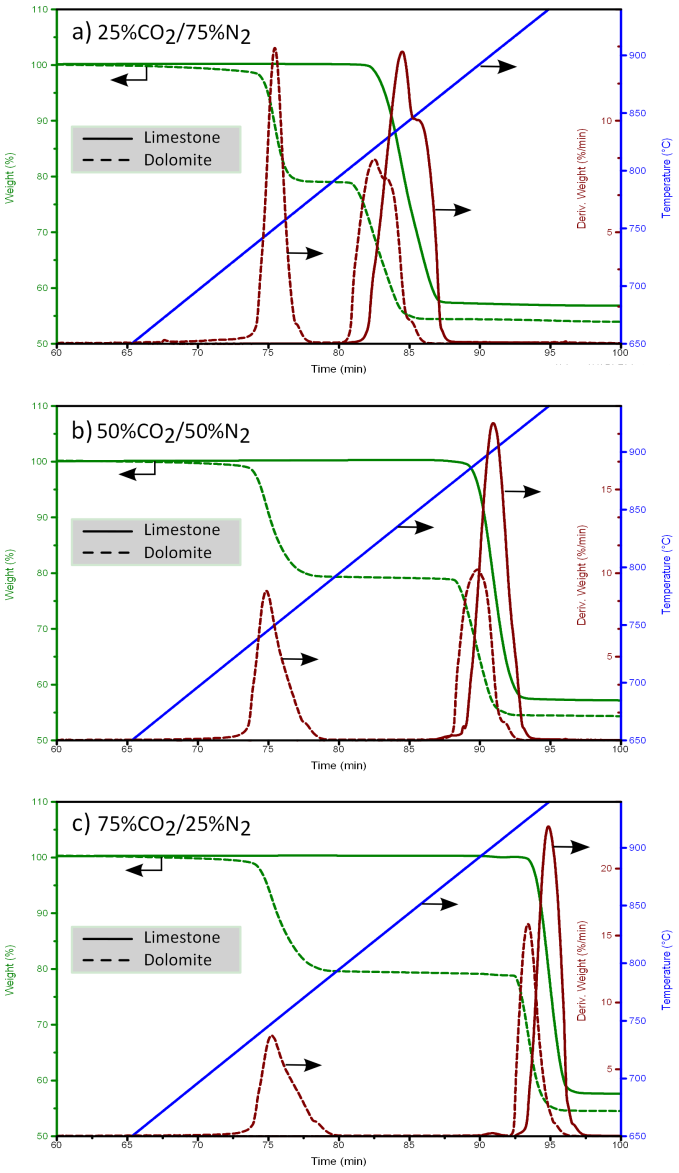

FIG. 4: Thermograms obtained for dolomite and limestone decomposition during calcination at atmospheric pressure under CO_2/N_2 gas mixtures at diverse CO_2 concentrations as indicated.

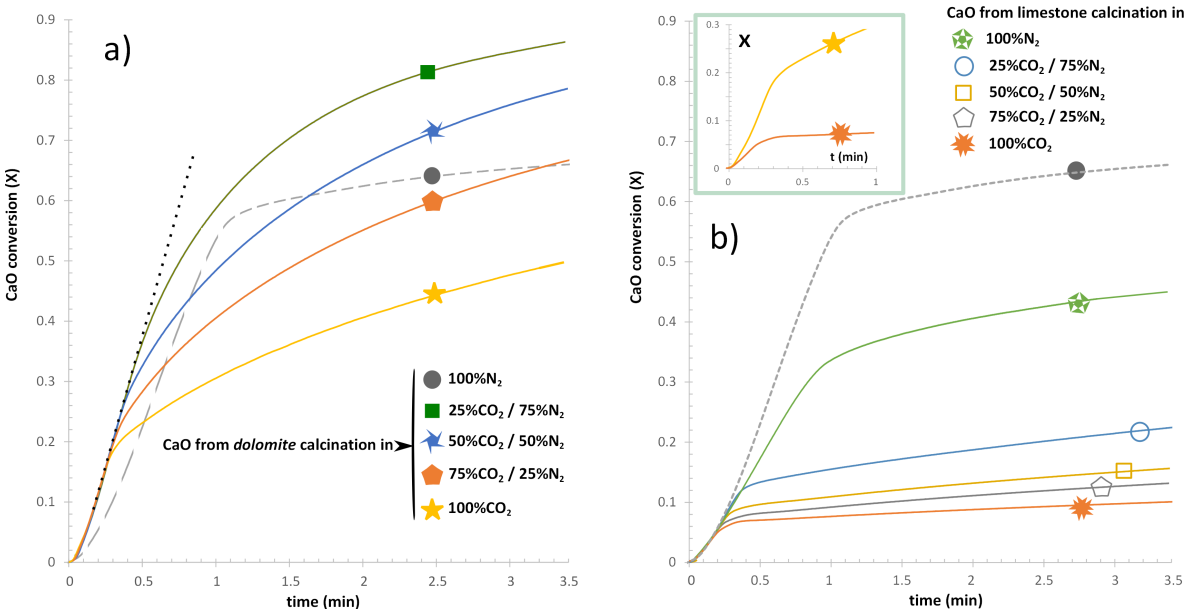

FIG. 5: Time evolution of CaO conversion during carbonation (650°C, 15%CO_2/85%N_2 vol/vol) of calcined dolomite (a) and limestone (b) samples carried out by in-situ TGA immediately after calcination under diverse CO_2/N_2 mixtures as indicated. For comparison, results for CaO derived from dolomite calcined in N_2 (dashed line) are shown in the main graph of b) and for dolomite calcined under CO_2 in the inset. The deviation from the dotted straight line in a) determines the boundary between carbonation regimes controlled by reaction at the surface of the solids and by solid-state diffusion.

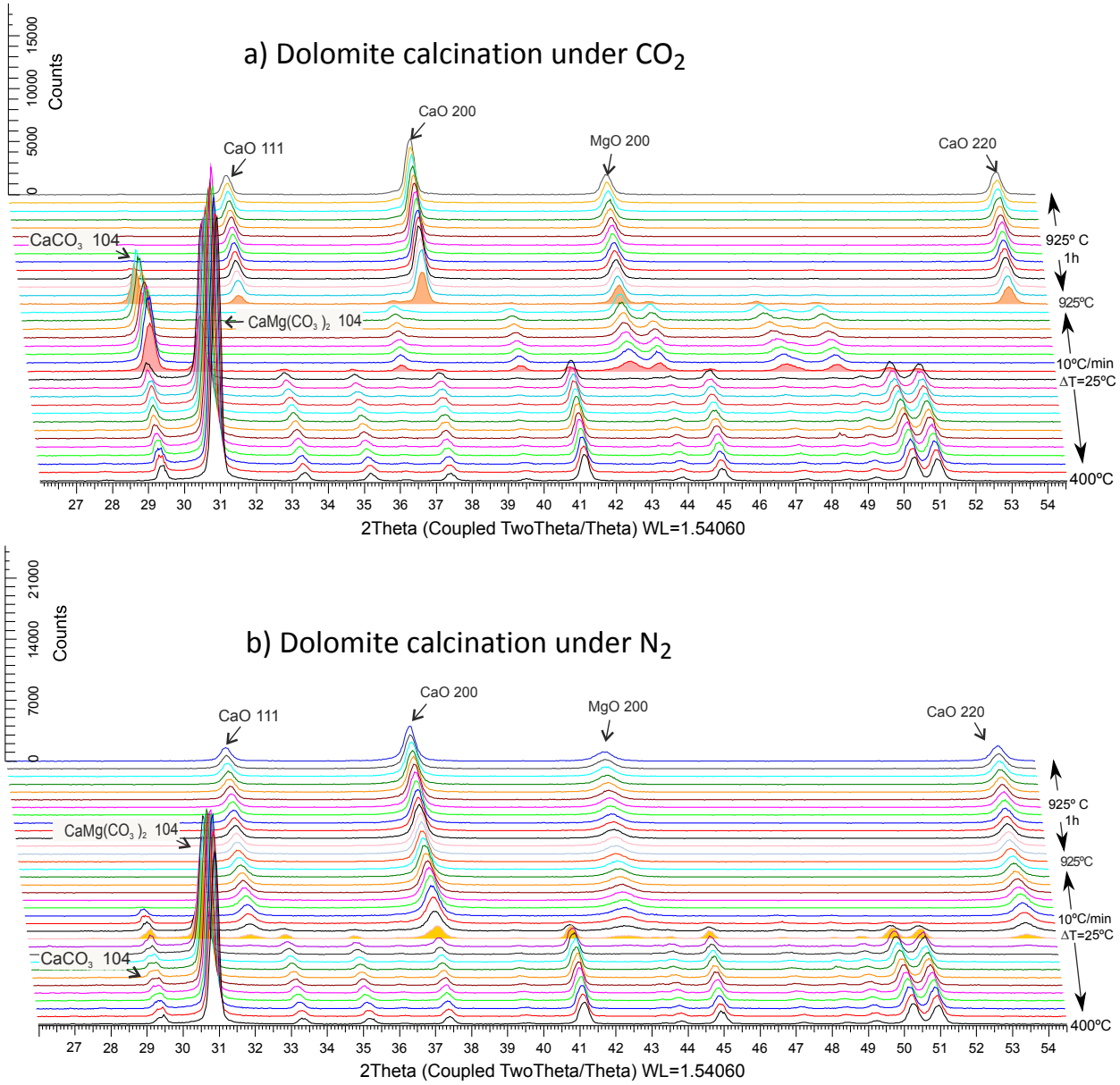

FIG. 6: XRD scans obtained during in-situ calcination of dolomite under pure CO_2 (a) and N_2 (b) atmospheres. Main Bragg peaks of dolomite ($CaMg(CO_3)_2$), calcite ($CaCO_3$), lime (CaO), and periclase (MgO) are indicated. The shadowed scans correspond to the observed onset of first and second decomposition stages under CO_2 (a) and direct decomposition under N_2 (b).

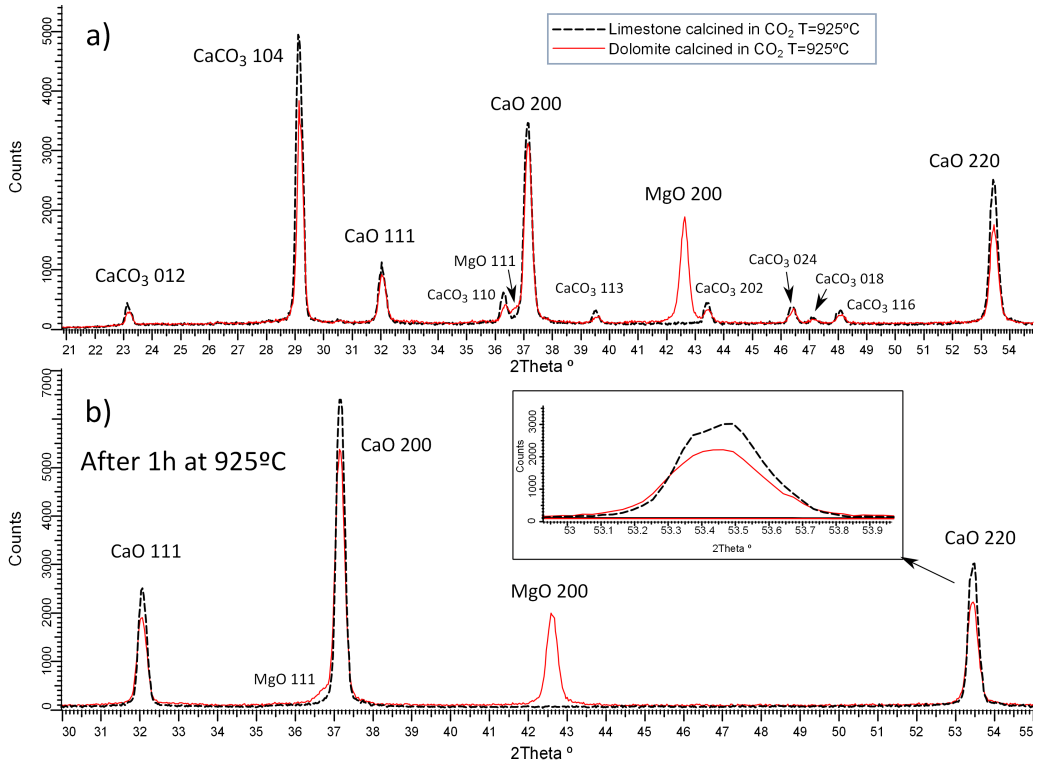

FIG. 7: XRD scans obtained during in-situ calcination of limestone and dolomite under pure CO_2. a) Just at the end of the temperature ramp (10°C/min) at $T = 925$°C. b) After 1h at 925°C from the end of the temperature ramp. The inset in b) is a zoom of the CaO 220 peak. Bragg reflection peaks of calcite ($CaCO_3$), lime (CaO), and periclase (MgO) are indicated.

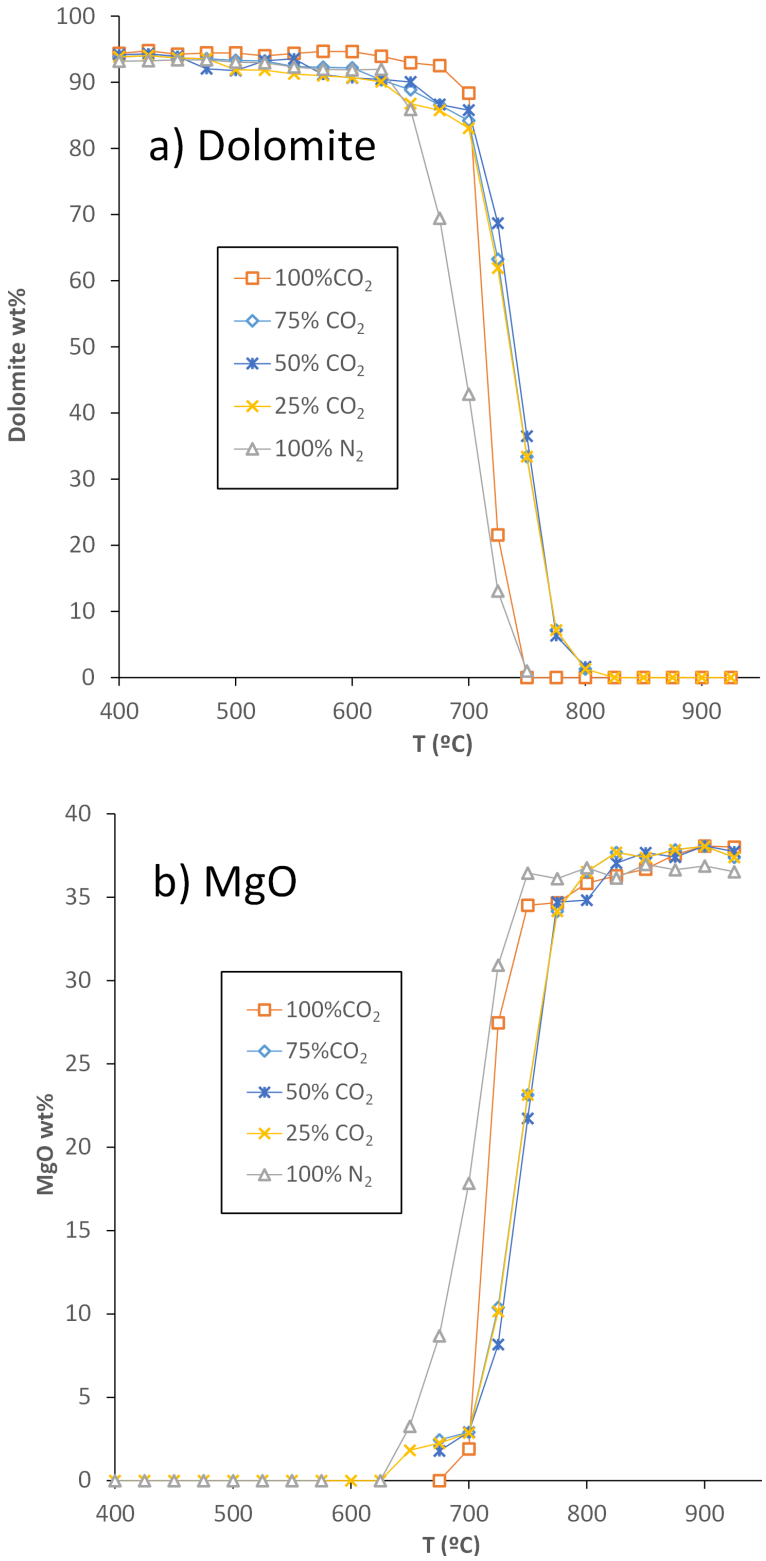

FIG. 8: Evolution with temperature of the wt% for dolomite (a) and MgO (b) during in-situ XRD calcination calculated by means of a Rietveld quantitative analysis for calcination tests under atmospheres of diverse CO_2 concentrations as indicated.

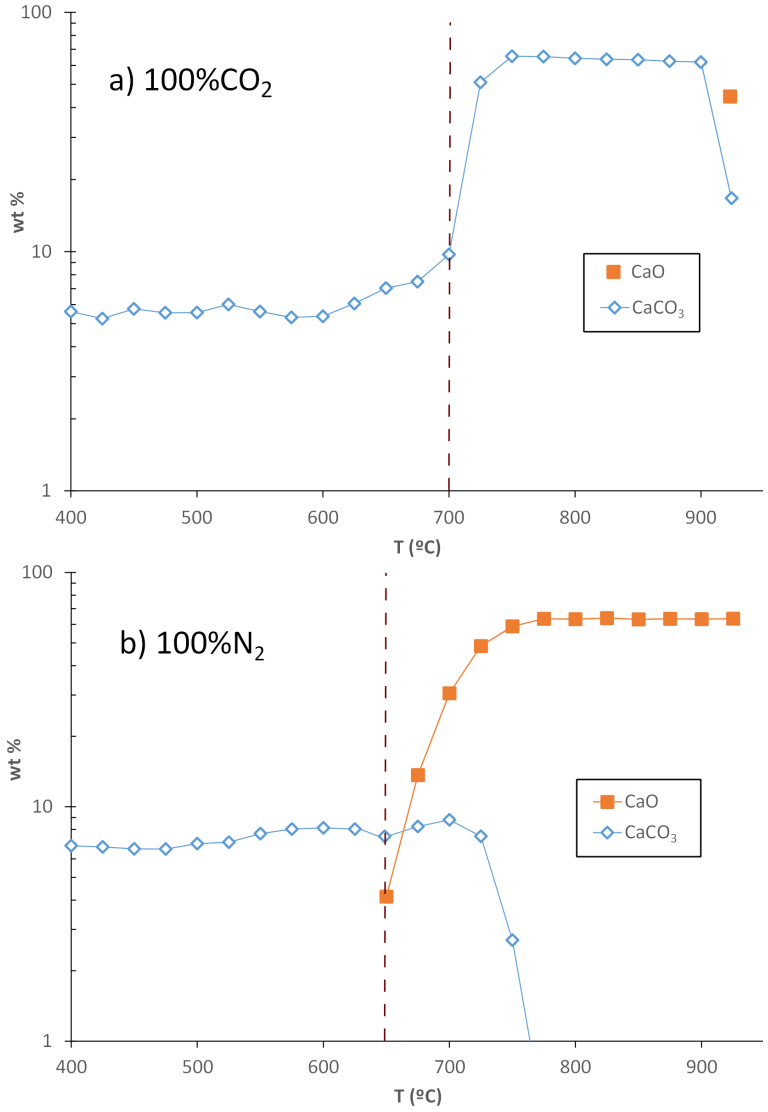

FIG. 9: Evolution with temperature of the wt% for $CaCO_3$ and CaO during in-situ XRD calcination. Calculated by Rietveld quantitative analysis for calcination tests under carried out under pure CO_2 (a) and N_2 (b). The vertical dashed line indicates the temperature at which the presence of MgO is first detected as indicative of the initiation of half-decomposition.

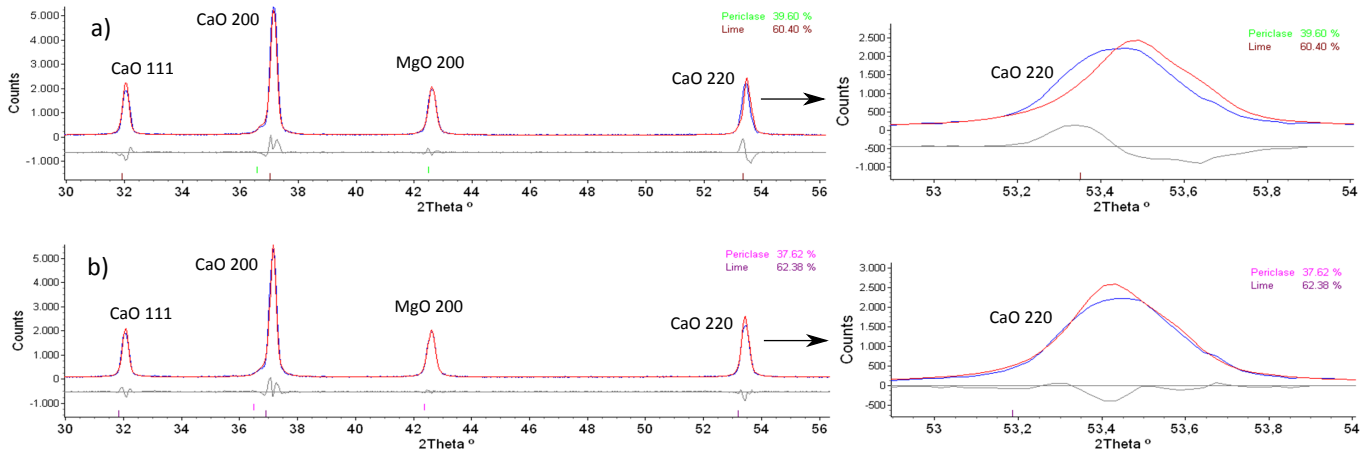

FIG. 10: Experimental diffractogram (blue) obtained for calcined dolomite in pure CO_2 (after 1h at 925°C from the end of the temperature ramp) and Rietveld best fits (red) for pure CaO and MgO phases (a) and allowing for the presence of Mg and Ca impurities in the oxides (b). The bottom grey line shows the deviation between the best fits and experimental diffractogram. Rietveld fitting parameters for pure CaO and MgO phases in a) are: 39.6wt% MgO (SD=0.39), 60.40wt% CaO (SD=0.39), GOF=1.98, Rwp=14.27, RBragg(MgO)=1.376, RBragg(CaO)=6.115. Rietveld fitting parameters allowing for Ca and Mg occupations in CaO and MgO, respectively in b) are: 37.62wt% $Mg_{1-x}Ca_xO$ with $x = 0$ (SD=0.023) and 62.380wt% $Ca_{1-y}Mg_yO$ with $y = 0.138$ (SD=0.014), GOF=1.47, Rwp=10.62, RBragg(MgO)=0.432, RBragg(CaO)=4.133. Right side figures show a zoom of the CaO 220 Bragg reflection peak.

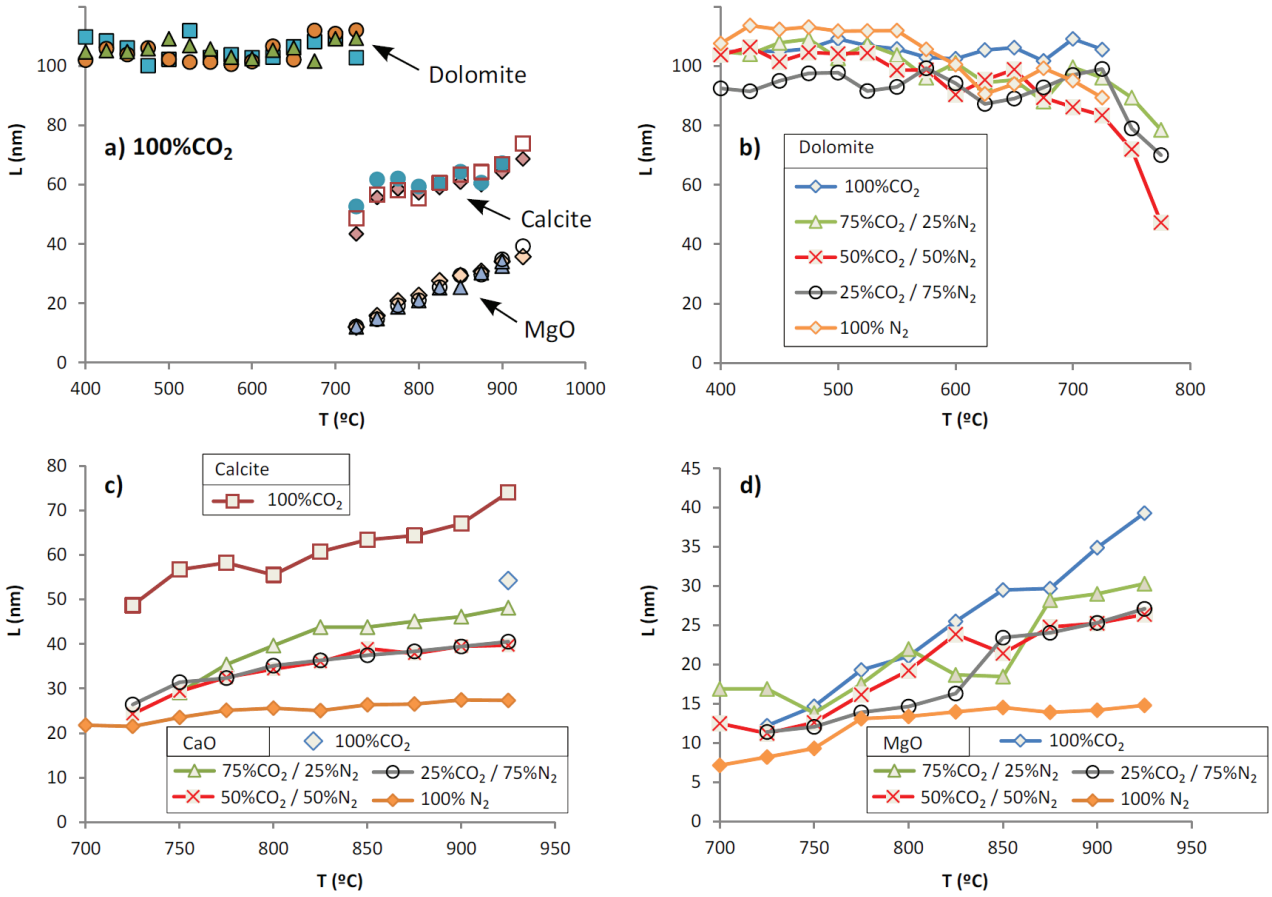

FIG. 11: CaO crystallite size L (calculated from Le Bail analysis of in-situ XRD diffractograms) of dolomite, calcite, CaO and MgO during decomposition of dolomite as a function of temperature (increased at 10°C/min). Calcination tests are carried out at atmospheric pressure under diverse CO_2/N_2 mixtures as indicated. Figure a) shows data from independent tests of dolomite calcination under pure CO_2 demostrating reproducibility.

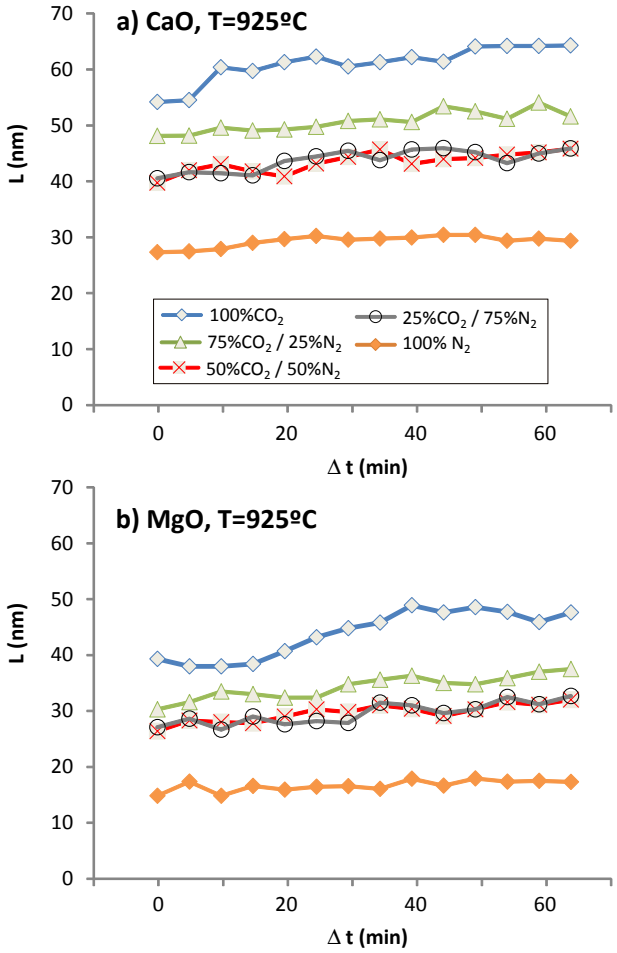

FIG. 12: Crystallite size L (calculated from Le Bail analysis of in-situ XRD diffractograms) of CaO (a) and MgO (b) during the isotherm at 925°C at the end of the temperature ramp. Calcination tests are carried out at atmospheric pressure under diverse CO_2/N_2 gas mixtures as indicated.

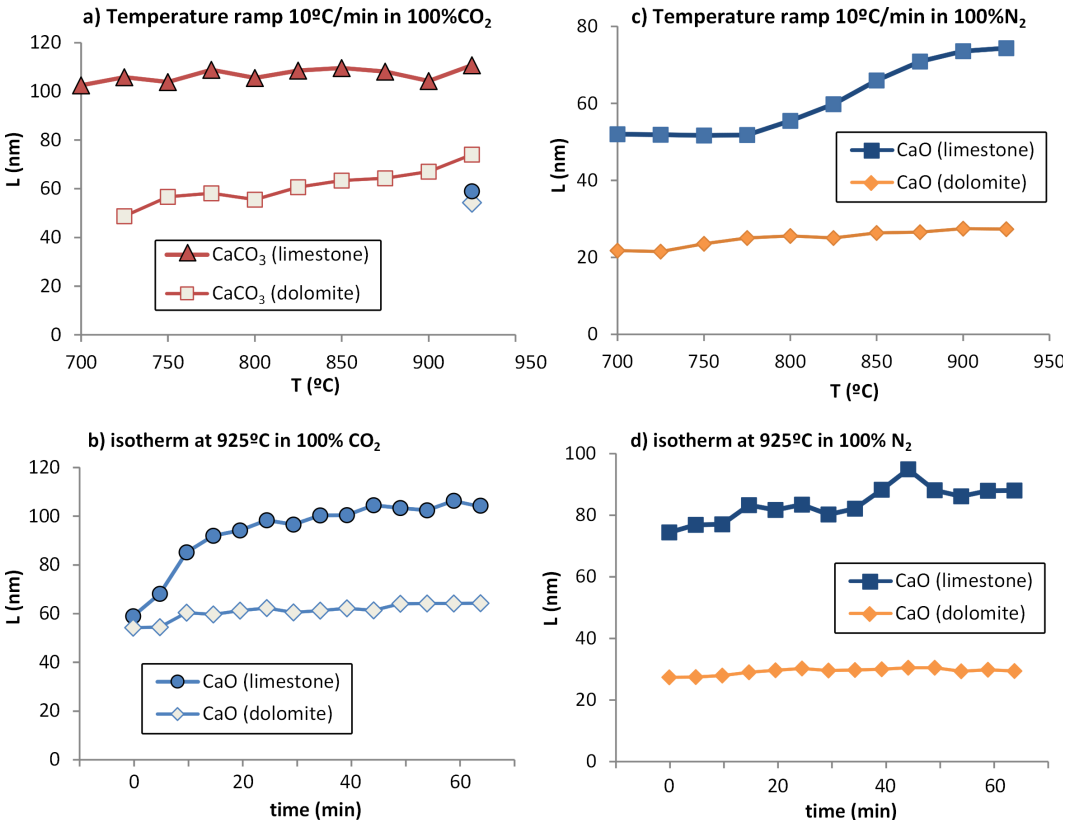

FIG. 13: Crystallite size L (calculated from Le Bail analysis of in-situ XRD diffractograms) of calcite ($CaCO_3$) and lime (CaO) obtained from dolomite and limestone calcination during the temperature ramp and the isotherm at 925°C as indicated. Calcination tests are carried out either under pure CO_2 or N_2 as indicated.

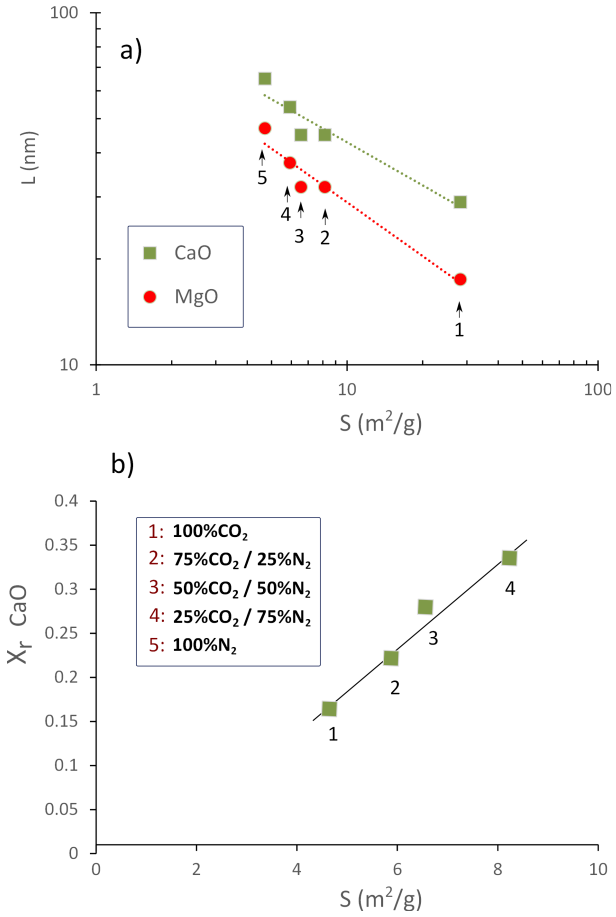

FIG. 14: a) Crystallite size L (calculated from Le Bail analysis of in-situ XRD diffractograms) of lime (CaO) and periclase (MgO) derived from dolomite calcination under environments of diverse CO_2 concentrations as indicated as a function of the BET surface area obtained from physisorption anlysis. b) CaO conversion in the reaction-controlled regime X_r as a function of the BET surface area for samples calcined under CO_2 at diverse concentrations as indicated. The dotted lines in a) represent the best power law fits. The solid line in b) is the best linear fit.